Disordering and grain boundaries of (Ni,Fe)Cr_2O_4 spinels from atomistic calculations

Alain Chartier,[a] Bogdan Golovchuk, Stéphane Gossé, and Laurent Van Brutzel
CEA, DEN, DPC, SCCME, F-91191 Gif-sur-Yvette Cedex, France

(Received 10 July 2013; accepted 11 September 2013; published online 1 October 2013)

A novel empirical potential has been developed to evaluate the thermodynamic stability of $Ni_{1-x}Fe_xCr_2O_4$ spinels. The simulations confirm the hypothesis that the $NiCr_2O_4$–$FeCr_2O_4$ pseudo-binary has normal structure spinel up to 1000 K and stabilizes as a solid solution. However, the disordering energy (normal to inverse spinel) is found higher for $FeCr_2O_4$ than for $NiCr_2O_4$ spinel. The formation energies of tilt, twist, and random grain boundaries have been calculated in pure $NiCr_2O_4$ and $FeCr_2O_4$. The same behavior has been found for both spinels. Detail analysis of the grain boundaries structure shows that the cation coordination number is a key parameter for the stability of the grain boundaries. With this criterion, we evidenced that the structural and energetic differences are caused only by nickel and iron cations. © *2013 AIP Publishing LLC*. [http://dx.doi.org/10.1063/1.4822262]

I. INTRODUCTION

$Ni_{1-x}Fe_xCr_2O_4$ spinels have been identified as part of the corrosion layer on nickel based alloys in pressurized water reactors (PWR).[1] The corrosion layer is also composed by other oxides and hydroxides. Cr_2O_3 is observed to form nodules at the interface between the substrate (alloy) and the spinels. Hydroxides are formed at the surface of the corrosion layer in contact with the primary water. The only continuous layer is the spinel layer.[1,2] Part of the corrosion process[1–3] relies on the electronic and ionic diffusion throughout this corrosion layer, and thus throughout the spinel layer. The system is expected to reach a steady state,[3] which is indeed out of equilibrium. However, the knowledge of the thermodynamic and kinetic properties of the $Ni_{1-x}Fe_xCr_2O_4$ spinels is required to understand and predict the corrosion of nickel based alloys.

Such knowledge leads to a detailed understanding of the point defect stability as already done in iron-chromium spinels.[4,5] For these spinels, it is known that a variation of the oxygen chemical potential does not affect the oxygen sub-lattice. The variation of the oxygen chemical potential is accommodated by the cation sub-lattice. For example, low oxygen chemical potential induces a hypo-stoichiometry of oxygen that is accommodated by an increase of cation interstitials. Conversely, high oxygen chemical potential induces a hyper-stoichiometry of oxygen that is accommodated by the occurrence of cation vacancies. However, in some cases, cation defects alone do not account for all the defect properties of the iron-chromium spinels.[4,6,7] Diffusion coefficients of cations adopt a V-shape as a function of the oxygen partial pressure in most iron-chromium spinels. This V-shape can easily be related to cation vacancies or interstitials concentration as a function of the oxygen partial pressure. Such V-shape is also observed for single crystals of magnetite.[5,8] Conversely, the diffusion coefficient in poly-crystalline magnetite is linear as a function of the oxygen partial pressure. As expected, grain boundaries (GBs) play a key role on the diffusion properties. In magnetite, grain boundaries enhance the diffusion at high oxygen chemical potentials. Surprisingly, GBs lower the cation diffusion at low oxygen chemical potentials.[5,8] In summary, thermodynamics gives us information about the nature and the concentration of the defects in the oxide layer at given conditions (e.g., oxygen partial pressure). These defects may migrate throughout the oxide layer, either in the bulk or throughout the GBs depending on the microstructure and/or on the oxygen chemical potential.

A recent thermodynamic CALPHAD modeling has been performed on the Ni–Fe–Cr–O quaternary system.[9] The $(Ni, Fe, Cr)_{3\pm x}O_4$ spinels are described by a four sub-lattice model as follow: $(Cr^{2+}, Cr^{3+}, Fe^{2+}, Fe^{3+}, Ni^{2+})_1$ $(Cr^{3+}, Fe^{2+}, Fe^{3+}, Ni^{2+}, VA)_2$ $(Cr^{2+}, Fe^{2+}, VA)_2$ $(O^{2-})_4$ (where VA sets for a vacancy). Because experimental measurements are missing, the $NiCr_2O_4$ and $FeCr_2O_4$ pseudo-binary composition is assumed to be a solid solution in this CALPHAD description. The $NiCr_2O_4$ and $FeCr_2O_4$ pseudo-binary composition is also considered to adopt normal structures up to the melting points. The diffusion coefficients of cations were measured back in the 1960s only for $NiCr_2O_4$.[10] The thermodynamic conditions are unclear,[10] and the role of the GBs is not discussed. To our knowledge, no study has ever been dedicated to the characterization of GBs in the $NiCr_2O_4$–$FeCr_2O_4$ system. Most experimental studies on spinel GBs concern $MgAl_2O_4$ and ferrites.[11–15] The experimental observations indicate a link between the crystal surface planes and the GBs planes, with twice more {1 1 1} planes compared to {1 0 0} planes in $MgAl_2O_4$. A similar observation is made for ferrite spinels,[12] the {1 0 0} planes being the third more frequent planes for GBs. Few structural details are available.[13,14] Finally, generic theoretical rules on GBs in oxides are useless,[16] as they describe

[a]alain.chartier@cea.fr

part of the experimental observations, and particularly in spinels.

The aim of the present work is to investigate (i) the ground state properties of bulk $Ni_{1-x}Fe_xCr_2O_4$ spinels and (ii) the stability and structure of some grain boundaries. These two parts will feed the general knowledge on the thermodynamic properties of the nickel based alloys corrosion layer. This study has been carried out with molecular dynamics simulations using fixed charges empirical potential. Such model can be considered accurate since most of the disordering in spinels AB_2O_4 was shown[17] to take origin from the electrostatic interactions between cations A and B. The first part of the work is dedicated to fit a new empirical potential, which describes the whole $Ni_{1-x}Fe_xCr_2O_4$ system. The empirical potential is then used to explore the effect of temperature on disordering. The second part of the work aims to investigate GBs. We study tilt, twist, and random GBs for both pure $NiCr_2O_4$ and $FeCr_2O_4$. We characterize these GBs using formation energies (γ), excess volumes (V_{excess}), density of miscoordinated cations (MCs), and coordination numbers (CNs).

II. STRUCTURE OF $NiCr_2O_4$ AND $FeCr_2O_4$ SPINELS

The $NiCr_2O_4$ and $FeCr_2O_4$ spinels do have magnetic behaviors at low temperatures. Their Curie points are, respectively, 320 K[18] and 88 K.[19] Due to their magnetic behaviors and their Jahn-Teller distortions, they show non-cubic structures below the Curie points. However, we will consider herein the cubic phase ($Fd\bar{3}m$) which occurs at temperatures higher than the Curie points. This simplification is relevant in our case since the temperatures of interest are above 300 K for the corrosion layers of nickel based alloys in PWR. This simplification allows us to use two-body empirical potential (see below), instead of more complex empirical potential needed to describe the Jahn-Teller effects.[20]

Spinels AB_2O_4 (where A and B are cations) are known to exhibit order-disorder transitions with temperature and/or with composition.[17,21] At low temperature, the $NiCr_2O_4$ and $FeCr_2O_4$ spinels are normal (quoted N in the following). The tetrahedral A site is filled by Ni or Fe in the formula AB_2O_4 while the octahedral B site is occupied by Cr. As the temperature increases, part of the cations may move in anti-site positions (the oxygen sub-lattice being unchanged) until eventually a complete inversion. The site inversion is quantified using the parameter x in the $(A_{1-x}B_x)_A(A_xB_{2-x})_BO_4$ formula, where the sub-scripts A (tetrahedral) and B (octahedral) indicate the sites. For example, for $x = 1$, there is a complete site inversion of the cations A to the site B and a random distribution of the A and B cations in the B site. The corresponding formula is $(B)_A(AB)_BO_4$ and is called an inverse spinel (quoted I in the following). For $x = 2/3$, there is a random distribution of the A and B cations in both A and B sites. The corresponding formula is $(A_{1/3}B_{2/3})_A(A_{2/3}B_{4/3})_BO_4$ and is called a disordered spinel (quoted D in the following). Indeed, the average CN of each cation varies as a function of the site inversion, and thus as a function of x. This can be used as alternative tool to quantify the effect of disorder, at the local scale. For normal spinel (N-spinel), the CN of nickel and iron atoms is CN(Ni) = CN(Fe) = 4, while for chromium atom is CN(Cr) = 6. In the case of inverse-spinel (I-spinel) CN(A) is 6 since all A cations sit on site B. The value of CN(B) is calculated by averaging over both A and B sites as previously done by Sickafus *et al.*[21] As half B cations are on site B and the other half on site A, the average CN(B) is thus 5 in I-spinel. Similarly, we calculate an average CN(A) and CN(B) of 5.33 for disordered-spinel (D-spinel).

III. EMPIRICAL POTENTIAL FITTING

The $NiCr_2O_4$ and $FeCr_2O_4$ spinels are described using two-body empirical potential inspired from the one used by Morooka *et al.* for $MgAl_2O_4$.[22] Part of the reason for this choice relies on its success to describe accurately the order-disorder transitions in $MgAl_2O_4$.[23,24] The empirical potential for the interaction between ions i and j at a distance of r is described as

$$U_{ij}(r) = \frac{q_i q_j}{4\pi\epsilon_0 r} + A_{ij}e^{-r/\rho_{ij}} - \frac{C_{ij}}{r^6} + D_{ij}\{e^{-2\beta_{ij}(r-r_0)} - 2e^{-\beta_{ij}(r-r_0)}\}. \quad (1)$$

The interactions are composed by a Coulomb, a Buckingham, and a Morse term. Each parameter has to be fitted in order to reproduce a set of chosen physical properties. We chose to use the same fractional charges, i.e., charge of +1.2 for Ni and Fe cations, +1.8 for chromium cation, and −1.2 for oxygen anion, like in the original empirical potential for $MgAl_2O_4$.[22] Note that since we use empirical potential with fixed charges, we are not able to describe the expected changes from Cr^{3+} to Cr^{2+} or Fe^{2+} to Fe^{3+} when site inversions occur. We also have kept the same oxygen-oxygen parameters and the same β and r_0 for the Morse potential proposed by Morooka *et al.*[22] (see Table I). The remaining free parameters of the empirical potential have been fitted with the GULP code[25] using a recursive method. The initial parameters were first chosen close to those of $MgAl_2O_4$.[22] We then achieved a fit using the cell and the internal parameters as target values for both normal $NiCr_2O_4$ and $FeCr_2O_4$ spinels. The fittings were done by minimizing the differences between calculated and experimental target values with the least-square method. Subsequently, we checked that both inverse spinels are less stable (i.e., have higher energies) than the corresponding normal structures. These relative stabilities are indeed the key for the suitability of the empirical potential for spinel. If the relative stabilities show that both normal spinels are more stable, then the recursive process is stopped. Otherwise, a new set of initial parameters is chosen, and the recursive process continues until the required relative stabilities. The parameters of the empirical potential obtained with this procedure are reported in Table I. Note that the Ni–Ni, Ni–Fe, and Fe–Fe Buckingham parameters are the same, as well as the Ni–Cr and Fe–Cr Buckingham parameters. The difference between both Ni and Fe cations relies on the short range Morse potential. The chromium and oxygen potential is unchanged between $NiCr_2O_4$ and $FeCr_2O_4$. Therefore, the present empirical potential is able to describe the whole pseudo-binary $Ni_{1-x}Fe_xCr_2O_4$ system (with x varying from 0 to 1).

TABLE I. Parameters of the empirical potential fitted to reproduce the properties of normal $NiCr_2O_4$ and $FeCr_2O_4$. The charges are +1.2 for Ni and Fe, +1.8 for Cr, and −1.2 for oxygen.

	A (eV)	ρ (Å)	C (eV Å^6)	D (eV)	β (Å^{-1})	r_0 (Å)
O–O	560.93434	0.360000	4.20			
O–Cr	689.77575	0.298944		1.3202651	2.00	1.80
O–Ni	284.09782	0.362661		2.4196868	2.00	1.80
O–Fe	118.05851	0.416163		1.3120262	2.00	1.80
Cr–Cr	1288.6597	0.118180				
Cr–(Ni, Fe)	1969.8009	0.353894				
(Ni, Fe)–(Ni, Fe)	113.63134	0.482105				

The calculated physical properties obtained using the new empirical potential are reported in Table II. Results show that the present empirical potential fairly describes the lattice parameters and the isothermal compressibility of both normal spinels on which the fit has been performed. Some other independent physical properties have been calculated in order to further assess the relevancy of the fitted potential. We have reported the vibrational entropy of both normal phases. They have been determined using the phonon spectra in the harmonic approximation, as implemented in the GULP code.[25] The calculated values are underestimated compare to the experimental data. However, their relative values follow a trend similar to the experimental data. We have also evaluated the thermal expansion coefficients of both normal spinels using molecular dynamics simulations at constant pressure and at temperatures ranging from 300 K up to 1800 K. This temperature range is below the experimental melting points of both $NiCr_2O_4$ and $FeCr_2O_4$ spinels.[9] The thermal expansion coefficients obtained show fair agreements with the experimental data available (see Table II).

IV. DISORDERING PROPERTIES AT 0 K

We have also investigated the disordering properties of both spinels. Part of the goal was to further compare the calculated properties with the thermodynamic data available.[9] The calculations were done in 448-atoms super-cells (that are $2 \times 2 \times 2$ the conventional cells). Each degree of inversion x considered (in the $(A_{1-x}B_x)_A(A_xB_{2-x})_BO_4$ compound) was sampled by at least 30 different configurations. Each configuration was built by a random distribution of the A and B cations in each tetrahedral and octahedral sub-lattices with respect to the inversion parameter x. Each structure was optimized by energy minimization. Finally, the properties (cell parameters, energies and bulk modulus) were calculated by averaging over the 30 different configurations mentioned above.

For both spinels, the calculations show that the cell parameters are slightly higher in the disordered and inverse phases with respect to the normal phases (see Table II). The bulk modulus values of the inverse phases are close to the ones of the normal phases for both spinels, while the values of the disordered phases are slightly lower. In fact, bulk modulus of both spinels show a minimum between the normal and inverse phases, as already observed in $MgAl_2O_4$.[26] However, the variations of the cell parameters and the bulk modulus remain smaller in the order of 0.5% and 3%, respectively. These variations are twice lower than those calculated in $MgAl_2O_4$.[26] The energy variation is much more significant. The inversion energy is calculated to be 0.07 eV/atom for $NiCr_2O_4$ close to the value of 0.1 eV/atom selected by Kjellqvist *et al.*[9] in their database for the CALPHAD description of the Ni–Fe–Cr–O quaternary system. This inversion energy is even higher for $FeCr_2O_4$ with a value of 0.2 eV/atom. But it is again in agreement with the selected data of 0.23 eV/atom for the CALPHAD model.[9]

Implicitly, these quantitate results mean that we capture most of the effect of site inversion on iron using empirical potential with fixed charges. This is particularly surprising for $FeCr_2O_4$ as iron atom is expected (i) to change from divalent to trivalent with site inversion and also (ii) to re-organize its spin configuration with the change from a tetrahedral to an octahedral environment.[38] However, analysis of experimental measurements using the bond valence shell model[34] shows

TABLE II. Comparison between calculated and experimental properties of $NiCr_2O_4$ and $FeCr_2O_4$ spinels in their normal (quoted N), disordered (quoted D), inverse (quoted I), amorphous (quoted A) structures. Bold values indicate the physical properties used for the empirical potential fitting.

		a (Å)		B_0 (GPa)		ΔU (eV/atom)		$S_{298\,K}$ (ACr_2O_4) (J mol^{-1} K^{-1})		α_V (10^{-5} K^{-1})	
		Calculated	Expt.	Calculated	Expt.	Calculated	Expt.	Calculated	Expt.	Calculated	Expt.
$NiCr_2O_4$	N	**8.284**	**8.305**[30]–8.315[27]	**231**	**204**[28]–333[33]	0.000		97	124[29]	2.2	2.1[30]
	D	8.298		224		0.075					
	I	8.297		228		0.072	0.106[9]				
$FeCr_2O_4$	N	**8.370**	**8.377**[31]–8.392[29]	**183**	**203**[32]–204[33]	0.000		104	146[29]	3.0	1.8–2.3[29]
	D	8.404		179		0.154					
	I	8.410		185		0.202	0.231[9]				

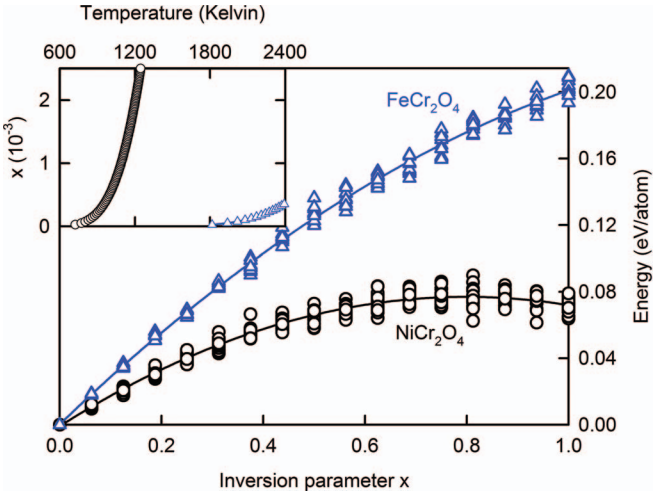

FIG. 1. Evolution of the potential energies (with respect to the normal structures) as a function of the inversion parameter x in $(A_{1-x}Cr_x)_A(A_xCr_{2-x})_BO_4$, with A = Fe (open blue triangles) or Ni (open black circles). For $x = 0$ the spinels are normal, while for $x = 1$ the spinels are inverse. The inset shows the evolution of the inversion parameter with temperature (see text for details).

that the change of the ionic charge with disorder remains relatively small at around 0.1 $|e|$. The role played by ionic interactions was recently confirmed by *ab initio* calculations for many different spinels.[17] This might explain the fair description obtained using empirical potential with fixed charges.

The evolution of the energy as a function of the inversion parameter is quite different for each spinel (see Figure 1). The energy of $FeCr_2O_4$ shows a monotonic increase with the inversion parameter x up to 0.2 eV/atom. Conversely, the energy of $NiCr_2O_4$ shows a maximum of 0.076 eV/atom at x = 0.8 before decreasing. The slopes of the energies at x = 0 on Figure 1 (multiplied by the number of atoms in AB_2O_4 formula, i.e., 7 to rescale to integer number of atoms) correspond to the anti-site formation energies of both compounds. The anti-site formation energies are, respectively, 1.6 and 2.4 eV for $NiCr_2O_4$ and $FeCr_2O_4$, higher than the one found in $MgAl_2O_4$ of 0.64 eV,[35] but close to the one of 1.6 eV for $ZnCr_2O_4$.[36] These values are consistent with the lower energy of disordering of $NiCr_2O_4$ compared to $FeCr_2O_4$.

These formation energies may be related to the CN departure of each cation from its ideal value, as suggested by Reznitskii.[37] The optimal CN is related to the ionic radius of a specific cation. The departure from the optimal CN is indeed endothermic. The energetic cost can be so high that it may hinder some excessive departure from the optimal CN. Here, the optimal CN of Cr^{3+} is 6, as for example in Cr_2O_3. Usually, it is also 6 for Fe^{2+}. This is exemplified in the magnetite compound Fe_3O_4, where Fe^{2+} is in the octahedral site. For the $FeCr_2O_4$ spinel, both CNs of Fe^{2+} and Cr^{3+} are competing to sit on the octahedral site. The ground state of the $FeCr_2O_4$ spinel being the N-spinel, here the optimal CN for Fe^{2+} is 4 instead of the usual value of 6. For Ni^{2+}, the optimal CN ranges from 4 to 6. Again, like Cr^{3+} has to be 6, the optimal value of Ni^{2+} is 4 in $NiCr_2O_4$. Both nickel and iron anti-sites change CN from their optimal value (in spinel) of 4 to a value of 6. But the effect of the departure from the ideal CN is more pronounced for $NiCr_2O_4$ than for $FeCr_2O_4$. In fact, nickel atom accommodates CN changes with lower energetic penalty (1.6 eV for anti-site) than iron (2.4 eV). This relative softness of nickel atoms compared to iron atoms will be evidenced with grain boundaries latter on.

V. TEMPERATURE EFFECT ON THE $FeCr_2O_4$–$NiCr_2O_4$ SYSTEMS

The variation of the energy as a function of x may classically be written[38] with a quadratic dependence. This quadratic dependence is preferred here to the Landau description mentioned by Redfern[39] because we have direct access to the variation of energies ΔU_S with inversion x. ΔU_S can then be written as follows:

$$\Delta U_S = U_x - U_{x=0} = \alpha x + \beta x^2. \tag{2}$$

Fitting the energies with this equation (lines on Figure 1) allows us to extract $\alpha_{NiCr_2O_4} = 131.6$ kJ/mol, $\beta_{NiCr_2O_4} = -81.9$ kJ/mol (for a chemical cell, i.e., for $FeCr_2O_4$ or $NiCr_2O_4$ with exactly 7 atoms) and $\alpha_{FeCr_2O_4} = 330.4$ kJ/mol, $\beta_{FeCr_2O_4} = -63.1$ kJ/mol. Note that these values are very different from those obtained for $MgAl_2O_4$ spinel.[38,39] With the configurational entropy calculated using the Bragg-Williams approximations, we obtain the free energy G(T, x) at a given temperature T and for a site inversion x. The minimum free energy at a given temperature T is given by $\partial G(T, x)/\partial x|_T = 0$. We obtain then the evolution of disorder x as a function of temperature T as follows:

$$-RT \ln\left[\frac{x^2}{(1-x)(2-x)}\right] = \alpha + 2\beta x. \tag{3}$$

Results are reported in Figure 1. They show that the $NiCr_2O_4$ disordering is higher than in $FeCr_2O_4$ at a given temperature, as expected from the energy differences. At 1000 K, the inversion x is below 3×10^{-3} for both spinels. This means that both phases are mainly in the normal structure up to 1000 K. The effect of the size of the supercells has been checked using the cluster expansion technique, as done in other spinels recently.[54] Such a technique allowed investigating far bigger cells with a better statistical sampling. The results obtained using the cluster expansion technique confirm the fact that both phases are normal up to 1000 K. Therefore, we will consider only the normal phases for both spinels in the following.

Finally, we have investigated the mixing energy (potential energy) in the $NiCr_2O_4$–$FeCr_2O_4$ solid solution. We have limited ourselves to the mixing of Ni and Fe in the A site as the normal phases are stable up to 1000°. As done for the disordering, the configurations were randomly generated for x ranging from 0 to 1 in $Ni_{1-x}Fe_xCr_2O_4$. The results reported in Figure 2 show that the solid solution is almost ideal and close to be regular. The maximum excess energy is three orders of magnitude lower than for the system $FeCr_2O_4$–Fe_3O_4.[40] It is 21.8 J/mol by chemical cell (around 1.2×10^{-3} eV/atom) with a slight dis-symmetry. We have calculated (using again the Bragg-Williams approximation) that the miscibility gap induced by this excess energy disappears for temperatures higher than 5 K. In other words, $NiCr_2O_4$–$FeCr_2O_4$

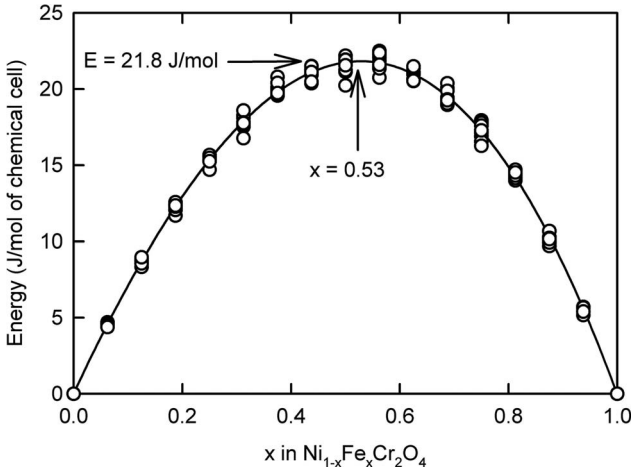

FIG. 2. Excess energy (potential energy) for the $Ni_{1-x}Fe_xCr_2O_4$ solid solution. The maximum value is 21.8 J/mol for the chemical cell at $x = 0.53$.

is mainly a solid solution. This result confirms what is currently used in the thermodynamic description of the Fe–Cr spinels.[9,41]

Indeed, the evaluations of the thermodynamic properties of both spinels are quite crude. The electronic and vibrational entropies are missing. However, the electronic entropy (the absolute value is below 10 $J\,mol^{-1}\,K^{-1}$)[38] and the vibrational entropy ($\sim$100 $J\,mol^{-1}\,K^{-1}$ at 300 K, see Table II) are negligible compared to the contribution of the configurational entropy and the potential energy for site inversions. Yet, the present empirical potential reproduces well the experimental inversion of potential energy of both $NiCr_2O_4$ and $FeCr_2O_4$. Both spinels are described by the present empirical potential as normal from low temperatures up to 1000° and stabilize as a solid solution. Therefore, the investigation of the grain boundaries will be limited to the normal $NiCr_2O_4$ and $FeCr_2O_4$ phases.

VI. GRAIN BOUNDARIES GENERATION AND TOOLS FOR ANALYSIS

We have investigated tilt, twist, and random grain boundaries of both $NiCr_2O_4$ and $FeCr_2O_4$ in their normal phases. Both tilt and twist grain boundaries were built using the coincidence-lattice site theory (CSL theory[42,43]). The rotation axis was chosen to be the [0 0 1] axis for both twist and tilt grain boundaries, although it is not the more observed experimentally, for example, in $MgAl_2O_4$ or MnZn ferrite spinels.[11,12] We have considered 6 tilt grain boundaries ($\Sigma5$, $\Sigma13$, $\Sigma17$, $\Sigma25$, $\Sigma29$, $\Sigma41$) and 3 twist grain boundaries ($\Sigma5$, $\Sigma13$, $\Sigma25$), with cell sizes reported on Table III. The number of atoms in the super-cells ranges from 20 000 up to 55 000. Note that each super-cell contains two grain boundaries because of periodic boundary conditions.

Each CSL grain boundary containing super-cell was relaxed with the following three steps procedure, using the LAMMPS code.[44] The super-cell was first optimized by minimizing the energy as a function of the 2D displacements of each crystal (as a rigid unit) along the GB plane. The optimization was then improved by a full energy minimization (of the ion positions and cell parameters) using the conjugated gradient method. The last step consisted in molecular dynamics calculations in the NPT ensemble at 300 K for 20 ps. The last two picoseconds were used to extract the average total energy, the average volume and the average grain boundary surface for each GB.

Random GBs were investigated using 200 000 atoms cubic super-cells which were divided into 27 cubes (each axis being divided by three). Each cube corresponds to bulk spinel whose crystallographic orientation (with respect to the super-cell reference) is randomly generated. The interfaces between each of these 27 cubes are consequently random. It means that 81 different random GB orientations were investigated for each spinel considered. Interestingly, this particular cubic geometry minimizes the effect of complicated junctions between grain boundaries. Using this geometry, it is also easy to determine the grain boundary surfaces in the whole super-cell.

TABLE III. Geometric features (misorientation angles, distances between GBs, and numbers of atoms), calculated formation energies γ(J/m^2) and excess volumes V_{excess} (10^{-10} m) at 300 K of the tilt, twist, and random grain boundaries for both $NiCr_2O_4$ and $FeCr_2O_4$. The distances of random GBs (with a star *) correspond to the edge length of the cubes (see text for details).

			GB dist. (Å)		γ (J/m^2)		V_{excess} (10^{-10} m)	
GB name	# Atoms	Angle (deg)	$NiCr_2O_4$	$FeCr_2O_4$	$NiCr_2O_4$	$FeCr_2O_4$	$NiCr_2O_4$	$FeCr_2O_4$
Tilt								
(310)[001]$\Sigma5$	40 320	36.86	78.8	79.8	4.1	3.4	0.13	0.56
(510)[001]$\Sigma13$	29 120	22.61	84.7	85.8	3.3	3.1	0.16	0.53
(530)[001]$\Sigma17$	22 848	61.92	48.4	49.0	2.5	2.3	0.16	0.34
(710)[001]$\Sigma25$	33 600	16.26	58.7	59.5	2.6	2.5	0.11	0.34
(730)[001]$\Sigma29$	38 976	46.39	63.3	64.1	2.9	2.7	0.18	0.46
(910)[001]$\Sigma41$	55 104	12.68	75.2	76.1	2.5	2.4	0.11	0.32
Twist								
(310)[001]$\Sigma5$	40 320	36.86	33.3	33.8	2.3	2.4	− 0.01	0.13
(510)[001]$\Sigma13$	46 592	22.61	33.3	33.8	4.5	6.0	0.15	0.67
(710)[001]$\Sigma25$	22 400	16.26	33.3	33.8	4.3	6.0	0.13	0.69
Random	198 464	...	42.1*	43.0*	2.3	2.5	− 0.09	0.05

Each of these super-cells was directly relaxed by molecular dynamics calculations in the NPT ensemble at 300 K for 20 ps. The average of total energy, volume, and grain boundary surface was then extracted from the last two picoseconds.

We have evaluated the grain boundary formation energy γ (J/m^2) and the excess volume per surface area V_{excess} (which is by definition an 1D length) by comparing the super-cell with (noted GB) and without (noted bulk) grain boundary using the following equations:

$$\gamma = \frac{E_{GB} - E_{bulk}}{2A} \tag{4}$$

and

$$V_{\text{excess}} = \frac{V_{GB} - V_{bulk}}{2A}. \tag{5}$$

E_{GB} and E_{bulk} are the grain boundary and the bulk energy, respectively; A represents the grain boundary surface area (the factor 2 is due to the periodic boundary conditions, which create 2 GBs per box). V is the volume while its subscripts are already defined.

The atomic structures of the GBs were also analyzed in terms of oxygen CNs for nickel, iron, and chromium atoms. The CNs were calculated by counting the number of oxygen ions around each cation in spheres of radius 2.45 Å. We considered slices of 1 nm thick centered on the GB interface for the CN analysis. This thickness was chosen because it includes most of the defects present at the GBs. We have also calculated the CN of each cation with respect to its ideal coordination number in the normal spinel. The CN deviation (ΔCN) was then evaluated as follows:

$$\Delta CN(\text{Ni, Fe}) = \frac{CN(\text{Ni, Fe}) - 4}{4} \tag{6}$$

and

$$\Delta CN(\text{Cr}) = \frac{CN(\text{Cr}) - 6}{6}. \tag{7}$$

We note that the CN deviation as a function of the inversion parameter x extends from 4 (tetrahedral site) up to 6 (octahedral site) for iron and nickel atoms. This means that the percentage of deviation ranges from 0% to 50% for both Ni and Fe atoms. This range is three times lower for chromium atoms (as a function of x). This comes from the fact that the CN deviation extends from 6 down to 5. The percentage of deviation goes from 0% down to −16.6% as a function of x. The miscoordinated cations at the GBs were also counted, and their density extracted, as previously done in yttria-stabilized zirconia (YSZ)[45] or in barium titanate perovskite ($BaTiO_3$).[46]

In present calculations, the distances between GBs are around 3.3 nm for twin GBs and range from 4.8 nm to 8.5 nm for twist GBs (see Table III). Note that the values mentioned for random GBs are the edge lengths of each of the 27 cubes of the super-cells. The distances between GBs used in our calculations are close to the thickness of the corrosion layer observed experimentally (of the order of 10 nm[1,2]). Present calculations on GBs are, therefore, performed at the required scale. This scale includes GB self-interactions that are known to be long range.[47] The self-interactions between grain boundaries cannot be avoided in our calculations because we use periodic boundary conditions. However, previous study[48] has shown that the error on GB formation energies is on the order of 0.2 J/m^2 for GB distanced by more than 5 nm. This is precisely the minimum value considered herein for tilt GBs. We also tried to consider roughly the same distances between GBs. This allows us to compare the relative stabilities of the grain boundaries and to ignore self-interactions. The estimation of the error on the excess volume (error coming from GB self-interactions) is evaluated to be less than 5×10^{-12} m. This error is roughly represented by the size of the symbols used on the Figures 3 and 4 for the sake of clarity.

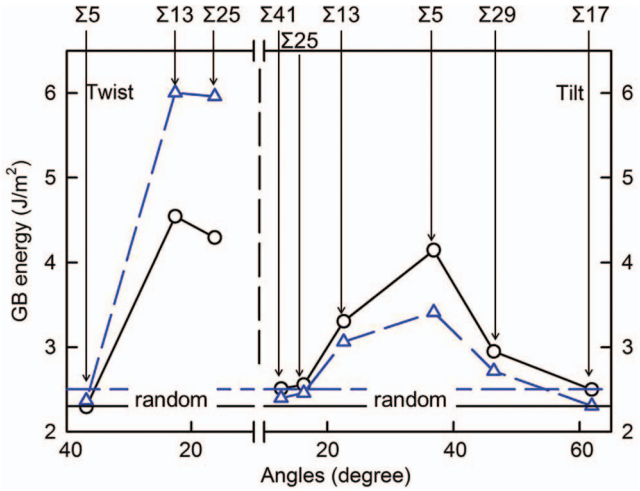

FIG. 3. Grain boundary formation energies (at 300 K) as a function of the misorientation angles for normal spinels $NiCr_2O_4$ (open black circles) and $FeCr_2O_4$ (open blue triangles). Twist grain boundaries are on the left side of the figure and tilt on the right side. The random grain boundaries are shown by the two horizontal lines at the bottom.

VII. GRAIN BOUNDARIES FORMATION ENERGIES AND LOCAL STRUCTURE

Results reported in Table III show that GB formation energies range from 2 to 6 J/m^2, and excess volumes are around

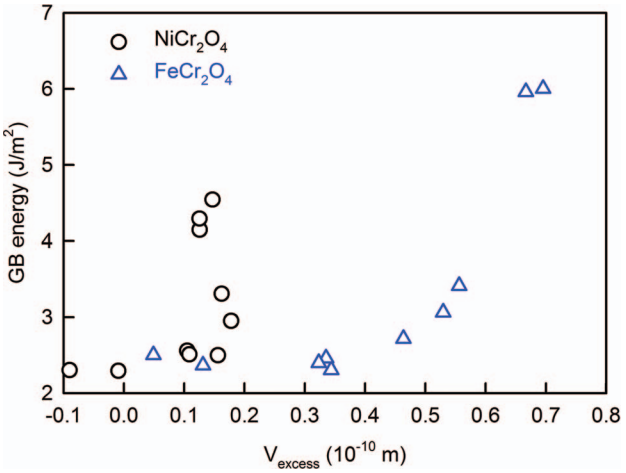

FIG. 4. Grain boundary formation energies as a function of the excess volumes (unit is 10^{-10} m or 10^{-10} m^3/m^2) for normal spinels $NiCr_2O_4$ (open black circles) and $FeCr_2O_4$ (open blue triangles).

TABLE IV. Grain boundaries formation energies γ (J/m^2), number density of miscoordinated cations (nm^{-2}), coordination number (CN), and percentages of deviation (ΔCN) (see text for definition) for both $NiCr_2O_4$ and $FeCr_2O_4$.

	γ (J/m^2)		MC (nm^{-2})		Ni		Cr in $NiCr_2O_4$		Fe		Cr in $FeCr_2O_4$	
	$NiCr_2O_4$	$FeCr_2O_4$	$NiCr_2O_4$	$FeCr_2O_4$	CN	ΔCN	CN	ΔCN	CN	ΔCN	CN	ΔCN
Tilt												
Σ5	4.1	3.4	12.1	8.5	4.22	+5.6%	5.90	−1.7%	3.96	−1.0%	5.90	−1.9%
Σ13	3.3	3.1	8.0	6.8	4.12	+2.9%	5.93	−1.1%	3.95	−1.4%	5.93	−1.6%
Σ17	2.5	2.3	6.0	6.8	4.04	+1.0%	5.93	−1.2%	3.93	−1.8%	5.93	−1.2%
Σ25	2.6	2.5	6.0	6.1	4.09	+2.2%	5.95	−0.8%	3.96	−1.1%	5.90	−1.1%
Σ29	2.9	2.7	9.4	8.4	4.12	+2.8%	5.91	−1.5%	3.95	−1.2%	5.94	−1.8%
Σ41	2.5	2.4	8.4	7.1	4.17	+4.4%	5.95	−0.9%	3.93	−1.7%	5.89	−0.9%
Twist												
Σ5	2.3	2.4	7.0	6.2	4.14	+3.4%	5.95	−0.9%	4.01	+0.2%	5.93	−1.2%
Σ13	4.5	6.0	13.3	11.6	4.35	+8.7%	5.92	−1.3%	4.01	+0.2%	5.86	−2.3%
Σ25	4.3	6.0	11.8	11.7	4.31	+7.9%	5.93	−1.2%	4.03	+0.6%	5.86	−2.3%
Random	2.3	2.5	11.2	7.7	4.05	−1.3%	5.92	−1.7%	3.98	−0.1%	5.91	−1.5%

10^{-11} m. These orders of magnitude are in agreement with the theoretical evaluation for Mg_2SiO_4 forsterite[49] as well as for Al_2O_3.[50,51] The calculated GB formation energies have been plotted in Figure 3 as a function of the misorientation angles for both $NiCr_2O_4$ and $FeCr_2O_4$. We have reported the GB formation energies of random GBs as lines, as they do not have any specific angle. We observe that the behaviors of the GB formation energies are similar for $NiCr_2O_4$ and $FeCr_2O_4$. The general shape of the GB formation energies as a function of the misorientation angle is also similar to those of NiO or MgO,[52] for both twist and tilt GBs. Among the CSL GBs investigated, tilt Σ17, Σ25, Σ41, and twist Σ5 show the lowest formation energies at around 2.5 J/m^2. Interestingly, the formation energies of random GBs lie in the same order of magnitude. The small differences between these GB energies are in the error bar, and cannot be considered as significant. This means, according to Rohrer,[52] that tilt Σ17, Σ25, Σ41, twist Σ5, and random GBs will represent the major part of the GB population, in equal quantity.

For both spinels the lower excess volumes correspond to the lower GB formation energies (see Figure 4). This is in agreement with the accepted theory where the increase of GB formation energies are usually related to the increase of the excess volume.[16] However, the evolution of the GB formation energy as a function of the excess volume is clearly not linear as expected and differs between $NiCr_2O_4$ and $FeCr_2O_4$. For $NiCr_2O_4$, the GB formation energy increases drastically around 0.15×10^{-10} m and saturate at 0.2×10^{-10} m. We even obtain negative excess volume for the random GBs and for the twist Σ5 (see Table III). The negative value of the twist Σ5 remains in the error bar, and cannot be considered as really negative. For $FeCr_2O_4$, the GB formation energy does not increase until an excess volume of 0.5×10^{-10} m where it begins to increase rapidly. Therefore, it is difficult to extract a correlation between the excess volume and the GB formation energy.

Alternatively, other criteria using GB structural analysis can be used to determine a correlation with the GB formation energy. We observed that most of the MCs are located at the vicinity of the grain boundaries, as expected. The MCs lie in slices of roughly 1 nm thick around the GBs. This is true for all GBs. We also calculated the density of MC in these 1 nm thick slices. The MC density includes under- and over-coordinated cations. The values of MC density per surface area range from 6 nm^{-2} up to 13 nm^{-2} (see Table IV). This corresponds to the values obtained in YSZ and $BaTiO_3$ perovskite.[45,46] But unlike the YSZ and $BaTiO_3$, we have not found any clear correlation between the GB formation energy and the MC density. For example, the MC density for the random GB of $NiCr_2O_4$ is as high as the one of the tilt Σ5: 11.2 nm^{-2} and 12.1 nm^{-2}, respectively, while the formation energy is half: 2.3 and 4.1 J/m^2, respectively.

As proposed by Reznitskii:[37] the change in energy can be related to the coordination number variation. The detailed analysis of the CNs is reported in Table IV. The chromium CNs are for both spinels lower (negative ΔCN) than the ideal value of 6. The nickel CNs are higher then the ideal value of 4, whereas the iron CNs are lower than the ideal value in tilt GBs and slightly higher in the twist GBs. It is important to note that the CN deviation is more pronounced for nickel than iron cations.

To analyze closely the CN relation with GB formation energy, we have plotted the evolution of the GB formation energy as a function of the CN deviation (ΔCN: difference of the CN with the ideal value expressed in percentage) on Figure 5. Figure 5 evidences that there is a correlation between the ΔCN and the formation energy, for both spinels. For the chromium ΔCN, we observe that the formation energy increases rapidly as a function of the departure from the optimal coordination number (6). The energetic contribution of chromium cations is the same for both spinels, which is consistent with the use of a transferable empirical potential for chromium and oxygen in the $FeCr_2O_4$–$NiCr_2O_4$ systems. Similar correlations can be seen for nickel or iron cations (right of the Figure 5), with an increase of the energy as a function of the increase of the CN. However, the behavior is quite different between them: ΔCN is slightly negative for iron and really positive for nickel. Moreover, we observe that

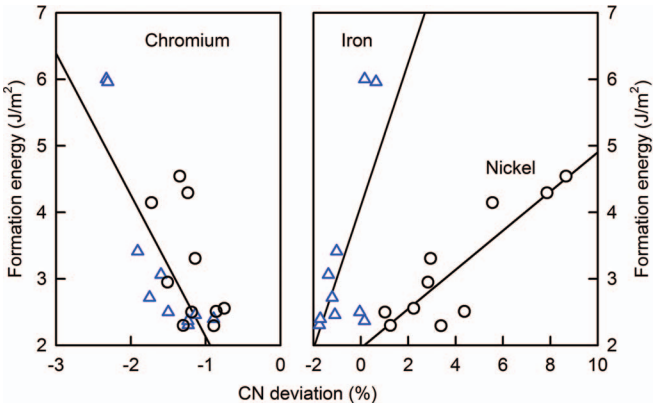

FIG. 5. Evolution of the formation energies (J/m^2) as a function of the ΔCN (CN deviation %). The figure on the left shows the evolution of the chromium atoms in both $NiCr_2O_4$ (open black circles) and $FeCr_2O_4$ (open blue triangles). The figure on the right shows the evolution of the nickel and iron atoms. Lines in both figures are just there to guide the eyes.

the slope of the formation energy as a function of ΔCN is much more pronounced for iron than for nickel cations. This can easily be related to the order-disorder transitions or to the anti-site formation energies of both spinels. We have shown previously that the anti-site formation energy is higher for $FeCr_2O_4$ (2.4 eV) than for $NiCr_2O_4$ (1.6 eV). Similarly, the energy for the order-disorder transition is higher in $FeCr_2O_4$ than in $NiCr_2O_4$ (see Figure 1). This means that the energetic contribution of Fe^{2+} is higher than the one of Ni^{2+}. It is less energetically favorable for the iron cations to deviate from its optimal CN of 4 than for the nickel cations (see Figure 5). Therefore, depending on the spinel chemistry, i.e., $FeCr_2O_4$ or $NiCr_2O_4$, the local arrangement at the GB is very different.

This analysis makes the cation CN a key parameter for the stability of GBs. We may then establish a link between the GB structures in terms of cation coordination number in the vicinity of the GB and the GB formation energies. Lower the departure from the ideal CN is, lower is the GB formation energy. As the role played by chromium is similar in $FeCr_2O_4$ and in $NiCr_2O_4$, it is likely that the structural and energetic differences are caused by nickel and iron cations only.

VIII. DISCUSSION AND CONCLUSIONS

We have reported here the investigation of the thermodynamic properties and grain boundaries properties of the $NiCr_2O_4$–$FeCr_2O_4$ system. The study has been done in the framework of molecular dynamics using fixed charged empirical potential. New empirical potential was fitted and assessed against structural, elastic, and thermal expansion properties. Interestingly, the assessment of the parameters leads to similar values for $NiCr_2O_4$ and $FeCr_2O_4$. The empirical potential was shown to well describe the disordering properties of the $NiCr_2O_4$–$FeCr_2O_4$ system. The values for complete inversion of both spinels are similar to those implemented in the CALPHAD modeling of the Ni–Fe–Cr–O system.[9] In particular, the inversion energy is much higher for $FeCr_2O_4$ than for $NiCr_2O_4$. We also show that the hypothesis currently done in CALPHAD modeling[9] for the $NiCr_2O_4$–$FeCr_2O_4$ pseudo-binary is relevant. These spinels are mainly normal up to 1000 K, and the system stabilizes as a solid solution along the $NiCr_2O_4$–$FeCr_2O_4$ pseudo-binary.

Different GBs have been investigated in $NiCr_2O_4$ and $FeCr_2O_4$ in their normal states. We have calculated 6 tilt grain boundaries ($\Sigma5$, $\Sigma13$, $\Sigma17$, $\Sigma25$, $\Sigma29$, $\Sigma41$), 3 twist grain boundaries ($\Sigma5$, $\Sigma13$, $\Sigma25$), and random grain boundaries. The rotation axis is the [0 0 1] axis for tilt and twist boundaries. The GB formation energies γ(GBs) have been calculated and related to structural parameters such as misorientation angles, excess volumes (V_{excess}), MC density, and CNs of cations.

Present work feeds again the well known fact[16] that the link between the formation energies γ(GBs) and the misorientation angles is not fully understood yet. The general trends of γ(GBs) in $NiCr_2O_4$ and $FeCr_2O_4$ are nevertheless similar. The minimum energies γ(GBs) are observed for random GBs, tilt $\Sigma17$, $\Sigma25$, and $\Sigma41$ and twist $\Sigma5$, at around 2.3–2.5 J/m^2. The increase of the excess volumes V_{excess} roughly follows the GB formation energies for $FeCr_2O_4$ unlike $NiCr_2O_4$ for which saturation is observed. The γ(GBs) and the V_{excess} could not be rationalized using MC density, as it was done recently for YSZ and $BaTiO_3$.[45,46] The CNs of cations have revealed to be the key criterion that correlates to the GB structure and formation energies γ(GBs) as well as the disordering. The CN evolutions are linear with the GB formation energies γ(GBs). The CN(Cr) evolution is identical in both spinels. It means that the contribution of chromium to the energy is similar for both spinels. However, the slopes for CN(Fe) and CN(Ni) are quite different. As a consequence, the energetic contributions of iron/nickel CNs to the formation energies are quite different, too. We observe that a change of the iron CN costs more in terms of γ(GBs) than a change of nickel CN. Therefore, the energy differences between $NiCr_2O_4$ and $FeCr_2O_4$ are caused by iron/nickel CNs only. This is supported by the fact that the energetic contribution of chromium is neutral, i.e., its contribution to γ(GBs) does not change with iron/nickel. The lower energetic cost of a change of the nickel CNs compared to the iron is also consistent with the disordering behavior of $NiCr_2O_4$ compared to $FeCr_2O_4$. The inversion energy is more than twice higher for $FeCr_2O_4$ compared to $NiCr_2O_4$. Again, since the chromium CNs change is the same for both spinels, iron/nickel cations only count for the difference.

The present work has been done using fixed charges empirical potential. This means that no electronic-magnetic properties can be described in $NiCr_2O_4$ and $FeCr_2O_4$ spinels, although these effects are known to exist in both.[18,19] Thus, any electrostatic polarization-charged defects are avoided at and in the vicinity of the grain boundaries. This might be why no depletion of iron/nickel atoms with respect to chromium atoms has been observed in both GB spinels, unlike what was seen by Nuns *et al.*[15] for $MgAl_2O_4$. In $MgAl_2O_4$, these authors also evidenced the occurrence of negative charges at the GBs. According to Nuns *et al.*,[15] those spatial charges arise from charged Mg vacancies in $MgAl_2O_4$. However, Paudel *et al.*[53] showed recently in some other spinels that anti-site and charge emission/absorption (between cation and anti-site) is in general preferable compared to cation (or oxygen) vacancies. Furthermore, the occurrence of vacancies is related to the

oxygen chemical potential.[5,8] Its role is not considered here, although its influence on the nature and on the concentration of point defects is of first order in bulk and GB spinel. Obviously, the charge and the nature of point defects are far from being well understood in bulk spinels, despite long standing studies.[5] The lack of knowledge on point defects at spinel GBs is even more present.

We may stand on the approximations that the ions in spinels have fixed charges, as described by the present empirical potential. This approximation is supported by the analysis of experimental observations,[34] which showed that the charge variation is less than 0.1 with anti-site exchange. Another recent *ab initio* study feeds the fixed charge approximation: Stevanović *et al.*[17] pointed out that the electrostatic interactions in spinels play a major role. Thus, present results obtained using fixed charge empirical potential evidence the relation between cation CN departure from its ideal value and the energy evolution in $NiCr_2O_4$ and $FeCr_2O_4$ spinels. This relation promoted by Reznitskii[37] stands for grain boundaries as well as for disordering properties. We may then establish a link between coordination number, disordering energy, and grain boundaries.

ACKNOWLEDGMENTS

Computational resources were provided by the Centre de Calcul et de Recherche et Technologie (CCRT). Computer time was also provided as part of the GENCI challenge project (allocation 2013-c97073).

[1]M. Sennour, L. Marchetti, F. Martin, S. Perrin, R. Molins, and M. Pijolat, J. Nucl. Mater. **402**, 147 (2010).
[2]L. Marchetti, S. Perrin, Y. Wouters, F. Martin, and M. Pijolat, Electrochim. Acta **55**, 5384 (2010).
[3]C. Bataillon, F. Bouchon, C. Chainais-Hillairet, J. Furhmann, E. Hoarau, and R. Touzani, J. Comput. Phys. **231**, 6213 (2012).
[4]J. Töpfer, S. Aggarwal, and R. Dieckmann, Solid State Ionics **81**, 251 (1995).
[5]R. Dieckmann, J. Phys. Chem. Solids **59**, 507 (1998).
[6]S. Aggarwal and R. Dieckmann, Phys. Chem. Miner. **29**, 695 (2002).
[7]S. Aggarwal and R. Dieckmann, Phys. Chem. Miner. **29**, 707 (2002).
[8]S. Aggarwal, J. Töpfer, T.-L. Tsai, and R. Dieckmann, Solid State Ionics **101–103**, 321 (1997).
[9]L. Kjellqvist, M. Selleby, and B. Sundman, Calphad **32**, 577 (2008).
[10]N. S. Gorbunov and V. I. Izvekov, Sov. Phys. Usp. **3**, 778 (1961).
[11]D. M. Saylor, B. El Dasher, Y. Pang, H. M. Miller, P. Wynblatt, A. D. Rollett, and G. S. Rohrer, J. Am. Ceram. Soc. **87**, 724 (2004).
[12]J.-S. Lee, D.-Y. Kim, J. Fleig, and J. Maier, J. Am. Ceram. Soc. **87**, 1895 (2004).
[13]C. B. Carter, Acta Metall. **36**, 2753 (1988).
[14]T. M. Shaw and C. B. Carter, Scr. Metall. **16**, 1431 (1982).
[15]N. Nuns, F. Béclin, and J. Crampon, J. Am. Ceram. Soc. **92**, 870 (2009).
[16] L. Priester, *Grain Boundaries: From Theory to Engineering*, Springer Series in Materials Science Vol. **172**, (Springer, 2013).
[17]V. Stevanović, M. d'Avezac, and A. Zunger, Phys. Rev. Lett. **105**, 075501 (2010).
[18]F. T. Docherty, A. J. Craven, D. W. McComb, and J. Skakle, Ultramicroscopy **86**, 273 (2001).
[19]M. Robbins, G. K. Wertheim, R. C. Sherwood, and D. N. E. Buchanan, J. Phys. Chem. Solids **32**, 717 (1971).
[20]S. M. Woodley, P. D. Battle, C. R. A. Catlow, and J. D. Gale, J. Phys. Chem. B **105**, 6824 (2001).
[21]K. E. Sickafus, J. M. Willis, and N. W. Grimes, J. Am. Ceram. Soc. **82**, 3279 (1999).
[22]S. Morooka, S. Zhang, T. Nishikawa, and H. Awaji, J. Ceram. Soc. Jpn. **107**, 1225 (1999).
[23]T. Yamamoto, A. Chartier, K. Yasuda, C. Meis, K. Shiiyama, and S. Matsumura, Nucl. Instrum. Methods Phys. Res. B **266**, 2676 (2008).
[24]A. Chartier, T. Yamamoto, K. Yasuda, C. Meis, and S. Matsumura, J. Nucl. Mater. **378**, 188 (2008).
[25]J. D. Gale and A. L. Rohl, Mol. Simul. **29**, 291 (2003).
[26]P. Shukla, A. Chernatynskiy, J. C. Nino, S. B. Sinnot, and S. R. Phillpot, J. Mater. Sci. **46**, 55 (2011).
[27]O. Crottaz, F. Kubel, and H. Schmid, J. Mater. Chem. **7**, 143 (1997).
[28]A. Sawaoka, S. Saito, K. Inoue, and T. Asada, Mater. Res. Bull. **6**, 97 (1971).
[29]D. Cubiciotti, J. Nucl. Mater. **201**, 176 (1993).
[30]G. Ottonello, Phys. Chem. Miner. **13**, 79 (1986).
[31]H. J. Levinstein, M. Robbins, and C. Capio, Mater. Res. Bull. **7**, 27 (1972).
[32]D. Fan, W. Zhou, C. Liu, Y. Liu, X. Jiang, F. Wan, J. Liu, X. Li, and H. Xie, J. Mater. Sci. **43**, 5546 (2008).
[33]D. Tromans and J. A. Meech, Minerals Eng. **15**, 1027 (2002).
[34]S. Surblé, G. Baldinozzi, D. Siméone, D. Gosset, and L. Thomé, Nucl. Instrum. Methods Phys. Res. B **266**, 3002 (2008).
[35]C. A. Gilbert, R. Smith, S. D. Kenny, S. T. Murphy, R. W. Grimes, and J. A. Ball, J. Phys.: Condens. Matter **21**, 275406 (2009).
[36]R. W. Grimes, D. Jason Binks, and A. B. Lidiard, Philos. Mag. A **72**, 651 (1995).
[37]L. A. Reznitskii, Inorg. Mater. **29**, 1166 (1993).
[38]H. S. C. O'Neill and A. Navrotsky, Am. Mineral. **68**, 181 (1983).
[39]S. A. T. Redfern, R. J. Harrison, H. S. C. O'Neill, and D. R. R. Wood, Am. Mineral. **84**, 299 (1999).
[40]H. S. C. O'Neill and A. Navrotsky, Am. Mineral. **69**, 733 (1984).
[41]V. A. Kurepin, Contrib. Mineral. Petrol. **149**, 591 (2005).
[42]H. Grimmer, W. Bollmann, and D. H. Warrington, Acta Crystallogr., Sect. A: Cryst. Phys., Diffr., Theor. Gen. Crystallogr. **30**, 197 (1974).
[43]A. F. Acton and M. Bevis, Acta Crystallogr., Sect. A: Cryst. Phys., Diffr., Theor. Gen. Crystallogr. **27**, 175 (1971).
[44]S. Plimpton, J. Comp. Phys. **117**, 1 (1995); see http://lammps.sandia.gov for distribution.
[45]N. Shibata, F. Oba, T. Yamamoto, and Y. Ikuhara, Philos. Mag. **84**, 2381 (2004).
[46]T. Oyama, N. Wada, and H. Takagi, Phys. Rev. B **82**, 134107 (2010).
[47]R. C. Cammarat and K. Sieradzki, Phys. Rev. Lett. **62**, 2005 (1989).
[48]A. Chartier, L. Van Brutzel, and M. Freyss, Phys. Rev. B **81**, 174111 (2010).
[49]O. Adjaoud, K. Marquardt, and S. Jahn, Phys. Chem. Miner. **39**, 749 (2012).
[50]T. Höche, P. R. Kenway, H.-J. Kleebe, M. Rühle, and P. A. Morris, J. Am. Ceram. Soc. **77**, 339 (1994).
[51]S. Fabris, S. Nufer, and C. Elsässer, Phys. Rev. B **66**, 155415 (2002).
[52]G. S. Rohrer, J. Mater. Sci. **46**, 5881 (2011).
[53]T. R. Paudel, A. Zakutayev, S. Lany, M. D'Avezac, and A. Zunger, Adv. Funct. Mater. **21**, 4493 (2011).
[54]C. Jiang, K. E. Sickafus, C. R. Stanek, S. P. Rudin, and B. P. Uberuaga, Phys. Rev. B **86**, 024203 (2012).